**Scientific Reports**

https://doi.org/10.1038/s41598-026-48525-z

**Article in Press**

# Investigation of perovskite solar cell temperature-dependent performance: a coupled opto-electro-thermal modeling approach

**Received: 16 August 2025**

**Accepted: 8 April 2026**

Published online: 17 April 2026

**Cite this article as: Suldozi R. & Razaghi M. Investigation of perovskite solar cell temperature-dependent performance: a coupled opto-electro-thermal modeling approach. *Sci Rep* (2026). https://doi.org/10.1038/s41598-026-48525-z**

**Reza Suldozi & Mohammad Razaghi**

We are providing an unedited version of this manuscript to give early access to its findings. Before final publication, the manuscript will undergo further editing. Please note there may be errors present which affect the content, and all legal disclaimers apply.

If this paper is publishing under a Transparent Peer Review model then Peer Review reports will publish with the final article.

ARTICLE IN PRESS

© The Author(s) 2026. **Open Access** This article is licensed under a Creative Commons Attribution-NonCommercial-NoDerivatives 4.0 International License, which permits any non-commercial use, sharing, distribution and reproduction in any medium or format, as long as you give appropriate credit to the original author(s) and the source, provide a link to the Creative Commons licence, and indicate if you modified the licensed material. You do not have permission under this licence to share adapted material derived from this article or parts of it. The images or other third party material in this article are included in the article's Creative Commons licence, unless indicated otherwise in a credit line to the material. If material is not included in the article's Creative Commons licence and your intended use is not permitted by statutory regulation or exceeds the permitted use, you will need to obtain permission directly from the copyright holder. To view a copy of this licence, visit http://creativecommons.org/licenses/by-nc-nd/4.0/.

# Investigation of Perovskite Solar Cell temperature-dependent performance: A Coupled Opto-Electro-Thermal Modeling approach

Reza Suldozi[a] and Mohammad Razaghi[b,*]

[a]Dept. of Physics, Faculty of Science, University of Kurdistan, Sanandaj, Iran
[b]Dept. of Electronics and Communication Engineering, Faculty of Engineering, University of Kurdistan, Sanandaj, Iran
[*]Corresponding author: m.razaghi@uok.ac.ir

**Abstract**

In this paper, we developed a opto-electro-thermal model using the 3D finite element method (FEM) in order to assess the temperature-dependent performance of perovskite solar cells (PSCs). The FEM-based model we developed is fully coupled, allowing us to model the optical absorption, charge transport, and heat generation processes all at once, which will provide a more precise evaluation of device performance. Four perovskite absorber materials ($MASnI_3$, $MAPbI_3$, $CsPbI_3$, and $CsSnI_3$) were evaluated based on three heat generation mechanisms: Joule heating, non-radiative recombination, and thermalization. Based on the proposed model, the extent of temperature rise within the device and its impact on device performance-primarily open-circuit voltage ($V_{oc}$) and power conversion efficiency (PCE) are assessed.

The simulation results show that the temperature-dependent performance of the PSC, varies according to the absorption layer material, as each type of absorber showed unique thermal behavior. In particular, $CsSnI_3$ exhibited notable temperature-dependent performance under thermal coupling, with a $V_{oc}$ reduction of only 2.38% and a PCE variation of 9.12%, showing a high photovoltaic response but higher temperature sensitivity under temperature variation compared to $CsPbI_3$.

keywords: PSCs, temperature-dependent performance, Joule Heat, Non-radiative Recombination Heat, Thermalization heat, Opto-electrical-Thermal Simulation.

## 1 Introduction

Perovskite Solar cells (PSCs) have emerged as promising candidates in next-generation photovoltaic technologies, offering both high power conversion efficiency (PCE) and inexpensive fabrication for potentially large-scale applications [1]. The stability and performance of PSCs is significantly affected by the absorber layer as it is vital to absorb light and generate free charges. However, the accumulation of heat produced in the absorber layer of the PSC negatively influences operating efficiency, accelerates materials degradation, and reduces the time in service/lifecycle. To increase the stability and desired operational life of PSCs in relevant applications, understanding the thermal performance of the absorber layer is essential [2].

Good thermal management is a key factor that affects both the performance and lifespan of PSCs. Elevated temperatures lead to undesirable effects such as enhanced ion migration, instability of the phases, and higher rates of non-radiative recombination, all of which negatively impact the efficiency of the solar cell over time [3]. As of now, thermal mitigation of PSCs has focused mainly on advancing material properties and device encapsulation techniques [4]. In improving the thermal management of PSCs, there is a need for a deeper understanding of the exact heat generation mechanisms taking place in the absorber layer. For improving stability of PSCs, it is important to analyze the mechanisms of heat generation from first principles [5]. Current studies highlight the importance of thermal modeling in PSCs. A 3D simulation using finite element method (FEM) demonstrated that high thermal conductivity electrodes, such as reduced graphene oxide (RGO), led to a significant reduction in thermal degradation and accumulation of temperature in active layers of the cell [6].

The influence of grain size, grain boundaries, and grain orientation on heat dissipation in PSCs is explored, with optimization strategies proposed for enhancing heat dissipation and temperature-dependent performance management [7]. An opto-electro-thermal model for perovskite/CZTSSe tandem solar cells is presented in [8], demonstrating that the majority of heat generation occurs in the bottom cell due to various loss mechanisms. Studies have shown that higher temperatures and thermal cycling enhance carrier recombination and reduce charge extraction from interfacial layers, leading to decreased efficiency and stability of the solar cells during extended thermal stress [3]. The scattering process of high-energy carriers in the conduction and valence bands generates heat, which can be a significant cause of early solar cell degradation [9].Studies have shown that the resistive heating and non-radiative recombination present in PSCs can result in device operating temperatures of 73–76°C with ZnO electron transport layer (ETL) and 80–84.5°C with $TiO_2$ ETL. Consequently, the effects of these processes may lead to further degradation and reduced stability of these devices [10].

Despite extensive research on heat generation in PSCs, prior studies have predominantly focused on Joule heat and heat from non-radiative recombination.

Joule heat is associated with ohmic losses of charge carriers moving through resistive layers/interfaces in the device. In contrast, non-radiative recombination heat involves the relaxation of excited charge carriers without emitting photons, usually through defects or traps. Although these mechanisms are well known in the literature, they do not fully cover all thermal effects in the absorber layer [11]. Thermal heat, generated from environmental influences and internal lattice vibrations, is one type that has received limited attention. This limitation emphasizes the need for a comprehensive preliminary assessment of all major heat sources that affect the performance of PSCs [12].

In this paper, we present an extensive approach for analyzing the heat generated in the absorber layer of PSCs by concentrating on three major sources: Joule heat, heat from non-radiative recombination, and thermalization heat. A simulation-based opto-electro-thermal coupling model is used to accurately simulate PSCs thermal behavior, thus providing an extensive account of thermal heat dissipation as well as heat generation in the absorber layer of PSCs. Previous studies, such as [13], [14], frequently used free triangular meshes to discretize the structure for modeling PSC. However, in our proposed modeling technique, a mapped mesh method is employed. A mapped mesh enhances modeling precision and elevates resolution, as the quantity and distribution of elements across layers are manually specified, hence refining interface modeling. The overall framework allows us to study the thermal behavior of PSCs with different absorber materials in a systematic way. We find that $CsPbI_3$ has the most stable temperature-dependent performance, showing minimal reductions in PCE and $V_{oc}$ under temperature variation, whereas $CsSnI_3$ demonstrates a strong photovoltaic response with higher temperature sensitivity, exhibiting a $V_{oc}$ decrease of 2.38% and a 9.12% variation in PCE. This paper is structured as follows: Section II describes the theoretical basis and the modeling methodology we developed, Section III describes and systematically examines the simulation results, and Section IV concludes the paper and summarizes deal with improvement of thermal management of PSCs.

## 2 Theory and modeling

Our multilayer device configuration is shown schematically in Figure 1. The top layer is the transparent conducting electrode (FTO), which is fluorine-doped $SnO_2$. Next comes the titanium dioxide ($TiO_2$) layer, thinned to be the ETL to assist with the extraction and flow of electrons. The perovskite material serves as the active layer, functioning as the light-absorbing layer responsible for charge generation. Located beneath the perovskite layer is the hole transport layer (HTL), composed of copper(I) thiocyanate (CuSCN), which allows the extraction and transfer of holes.

The metal electrode at the bottom is made of Au to assist with the collection of charge. The thickness of each layer can be seen in Table 1.

Table 1: The electrical and thermal parameters of PSC. [15],[16], [17],[18], [19],[20],[21]

| Parameter | FTO | $TiO_2$ | $CH_3NH_3PbI_3$ | $CH_3NH_3SnI_3$ | $CsSnI_3$ | $CsPbI_3$ | CuSCN | Au |
|---|---|---|---|---|---|---|---|---|
| Thickness [nm] | 50 | 50 | 200 | 200 | 200 | 200 | 600 | 100 |
| $\varepsilon_r$ | - | 9 | 6.5 | 8.2 | 8.4 | 6.3 | 10 | - |
| $N_c$ ($cm^{-3}$) | - | $1 \times 10^{19}$ | $1.66 \times 10^{18}$ | $1 \times 10^{18}$ | $2 \times 10^{18}$ | $2.5 \times 10^{18}$ | $1.79 \times 10^{19}$ | - |
| $N_v$ ($cm^{-3}$) | - | $1 \times 10^{19}$ | $5.41 \times 10^{18}$ | $1 \times 10^{18}$ | $2 \times 10^{18}$ | $2.5 \times 10^{18}$ | $2.51 \times 10^{19}$ | - |
| $\mu_e/\mu_h$ ($cm^2$/V s) | - | 20/10 | 50/50 | 1.6/1.6 | 2/2 | 10/10 | $1 \times 10^{-4} \sim 0.01$ | - |
| $\chi$ (eV) | - | 4 | 3.93 | 4.17 | 4.2 | 3.9 | 1.9 | - |
| $E_g$ (eV) | - | 3.2 | 1.55 | 1.3 | 1.3 | 1.73 | 3.4 | - |
| $N_A$ ($cm^{-3}$) | - | - | $5 \times 10^{13}$ | $3 \times 10^{16}$ | $2 \times 10^{16}$ | $5 \times 10^{16}$ | $5 \times 10^{18}$ | - |
| $N_D$ ($cm^{-3}$) | - | $5 \times 10^{18}$ | - | - | - | - | - | - |
| $\tau_n/\tau_p$ (ns) | - | 5/2 | 25/25 | 25/25 | 25/25 | 25/25 | 5/5 | - |
| $\rho$ ($kg/m^3$) | 5560 | 3900 | 4286.4 | 4500 | 4600 | 4700 | 2840 | 19300 |
| $K$ (W/mK) | 31 | 4.8 | 0.59 | 0.6 | 0.7 | 0.8 | 2.39 | 129 |
| $C_m$ (J/kgK) | 128 | 683 | 308 | 320 | 330 | 340 | 800 | 318 |

## 2.1 Optical modeling

The optical properties of PSC are modeled by utilizing the FEM-based wave optics, as outlined in [22]. The Helmholtz equation, derived from Maxwell's equations, governs the propagation of electromagnetic waves in the device:

$$\nabla \times (\nabla \times \mathbf{E}) - k_0^2 \varepsilon_r \mathbf{E} = 0, \tag{1}$$

where $\mathbf{E}$ is the electric field, $k_0 = \frac{2\pi}{\lambda}$ is the wave vector in free space, and $\varepsilon_r = (n - i\kappa)^2$ is the complex relative permittivity, with $n$ and $\kappa$ being the refractive index and extinction coefficient, respectively. The optical generation rate $G_{\text{photo}}(\lambda)$ is calculated as:

$$G_{\text{photo}}(\lambda) = \frac{\varepsilon'' |\mathbf{E}|^2}{2\hbar}, \tag{2}$$

where $\varepsilon''$ is the imaginary part of the dielectric permittivity and $\hbar$ is the reduced Planck constant.The total generation rate $G_{\text{tot}}$ is obtained by integrating $G_{\text{photo}}(\lambda)$ over the solar spectrum (300–1000 nm) [23]:

$$G_{\text{tot}} = \int_{\lambda_{\min}}^{\lambda_{\max}} G_{\text{photo}}(\lambda) d\lambda. \tag{3}$$

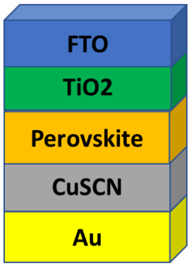

Figure 1: Schematic of the desired structure.

## 2.2 Electrical modeling

The electrical performance is simulated by solving the Poisson equation and the carrier continuity equations in a drift-diffusion model [24]:

$$\nabla \cdot (\varepsilon_0 \varepsilon_r \nabla \phi) = -q(p - n + N_D - N_A), \tag{4}$$

$$\frac{\partial n}{\partial t} = \frac{1}{q} \nabla \cdot \mathbf{J}_n + G_{\text{tot}} - U_n, \tag{5}$$

$$\frac{\partial p}{\partial t} = -\frac{1}{q} \nabla \cdot \mathbf{J}_p + G_{\text{tot}} - U_p, \tag{6}$$

where $\phi$ denotes the electrostatic potential, $n$ and $p$ are the electron and hole concentrations, $N_D$ and $N_A$ are donor and acceptor densities, and $U_n$ and $U_p$ are recombination rates for electrons and holes, respectively. Current densities $\mathbf{J}_n$ and $\mathbf{J}_p$ are provided by the drift-diffusion model:

$$\mathbf{J}_n = q\mu_n n\mathbf{E} + qD_n \nabla n, \tag{7}$$

$$\mathbf{J}_p = q\mu_p p\mathbf{E} - qD_p \nabla p, \tag{8}$$

where $\mu_n$ and $\mu_p$ are the electron and hole mobilities, and $D_n$ and $D_p$ are electron and hole diffusion coefficients.

## 2.3 Thermal model

The heat transfer model is used to simulate the thermal properties of the PSC. The heat equation is solved to determine the temperature profile [25]:

$$\rho C_p \frac{\partial T}{\partial t} + \nabla \cdot (-k \nabla T) = Q \tag{9}$$

where $\rho$ is the material density, $C_p$ is the specific heat capacity, $k$ is the thermal conductivity, and $Q$ is the rate of total heat generation. In the thermal model, natural convection and radiation are considered as heat dissipation mechanisms due to the cell's contact with air [26]:

$$Q_{\text{conv}} = h(T - T_{\text{amb}}) \tag{10}$$

$$Q_{\text{rad}} = \epsilon\sigma(T^4 - T_{\text{amb}}^4) \tag{11}$$

where $h$ is the convective heat transfer coefficient, $\epsilon$ is the emissivity, and $\sigma$ is the Stefan-Boltzmann constant and $T_{\text{amb}}$ ambient temperature.

### Heat Sources in the Thermal Module

Three primary heat sources of Joule heat, non-radiative recombination heat, and thermalization heat are considered in the thermal module [27]:

### Joule Heat

Joule heat arises due to resistive losses as carriers move through the device under an electric field. The Joule heat density $H_{\text{Joule}}$ is given by:

$$H_{\text{Joule}} = \mathbf{E} \cdot \mathbf{J} \tag{12}$$

where $\mathbf{J} = \mathbf{J}_n + \mathbf{J}_p$ is the total current density.

### Non-Radiative Recombination Heat

Non-radiative recombinations, such as Shockley-Read-Hall (SRH) recombination, release energy as heat. The non-radiative recombination heat density $H_{\text{SRH}}$ is:

$$H_{\text{SRH}} = (E_g + 3k_B T)U_{\text{SRH}} \tag{13}$$

where $E_g$ is the material bandgap, $k_B$ is the Boltzmann constant, and $U_{\text{SRH}}$ is the SRH recombination rate:

$$U_{\text{SRH}} = \frac{np - n_i^2}{\tau_p(n + n_1) + \tau_n(p + p_1)} \tag{14}$$

where $n_i$ is the intrinsic carrier concentration, $\tau_n$ and $\tau_p$ are electron and hole lifetimes, and $n_1$ and $p_1$ are the electron and hole densities when the quasi Fermi level matches the trap energy.

### Thermalization Heat

Thermalization occurs when hot electrons, arising from high-energy photons that promoted them to the conduction band, lose their surplus energy and relax to the edge of the conduction band [11]. Thermalization heat density $H_{\text{th}}$ is given by:

$$H_{\text{th}} = \int (h\nu - E_g - 3k_B T)G_{\text{photo}}(\lambda)\, d\lambda \tag{15}$$

where $\nu$ is the light frequency.

These heat sources collectively contribute to the total heat generation $Q$ in the thermal model, enabling the analysis of temperature effects on PSC performance.

## 2.4 Coupling Method of the Three Modules

The coupling approach used in this study involves four steps. In our model, the starting temperature is set to ambient temperature (293 K). The first step is to use the optical model to calculate the wavelength-dependent photogeneration rate $G_{\text{photo}}(\lambda)$. The total photogeneration rate $G_{\text{tot}}$ is calculated by integrating the photogeneration rate across the solar spectrum. The second step is to apply the electrical model. This step includes utilizing the $G_{\text{tot}}$ and solving the Poisson and drift-diffusion equations to determine the distributions of carrier densities, electric fields, and current densities. Using these quantities, heat sources including Joule heat, non-radiative recombination heat, and thermalization heat are calculated.The third step is employing the thermal model, which incorporates the previously indicated heat sources, to calculate the temperature profile through the device structure using the heat transfer equation. The fourth and last step is to use the electrical model again to incorporate the new temperature profile calculated by the thermal model and update PSC's electrical characteristics. Using this systematic coupling approach, we can properly assess PSC performance by taking into account generated heat in the PSC structure.

To improve transparency and credibility, the intermediary outputs from each module are included in the "Supplementary Data": (i) Optical model: refractive index and extinction coefficient of perovskite materials, generation rate profile $G(z)$ as function of depth z; (ii) Electrical model: carrier densities as function of depth z, $n(z), p(z)$, electric field and current density distribution; (iii) Thermal model: temperature map. Each of these is referenced in detail in Figures (S1-S6). In this present coupled opto-electro-thermal model, several simplifying assumptions were made to allow the simulations to be performed. The bandgap energy ($E_g$) and carrier mobilities ($\mu_n, \mu_p$) were assumed to be invariant with temperature, and our approach did not incorporate defect or trap states of interfaces in the electrical simulations.

## 2.5 Mesh Structure

The tetrahedral meshing method has typically been employed as mentioned before in prior studies to model the performance of solar cells. This study employs a mapped meshing technique to enhance control over element distribution in the computational domain. This technique improves simulation performance by enhancing the quality of optical, thermal, and electrical models, increasing layer interface resolution, and facilitating solver convergence. The element sizes in our simulations vary from 52.2 nm to 2.24 nm, guaranteeing appropriate resolution levels needed.

We uses skewness and growth rate as the two parameters to assess the quality of the mesh. They are illustrated in Figure 2 As it is shown the skewness values were consistently close to 1, indicating that suitable quality mesh elements had been created. The growth rate remained constant at 1.35 to accommodate smooth transitions to neighboring elements. The mapped mesh divided the complete geometry into 14,756 elements and had an element quality of 0.85 on average, thus giving a high level of quality and an acceptable balance between solutions and computation cost. Not only does this approach improve fidelity in simulations, but it also allows for improved computation performance in comparison to free meshing methods; as such, this approach is appropriate for coupled optical-electrical-thermal studies in complex 3D structures like PSCs.

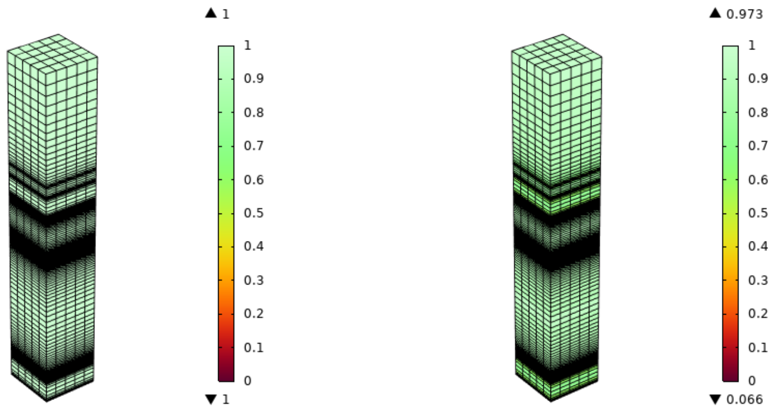

(a)

(b)

Figure 2: Mesh quality assessment showing (a) skewness and (b) growth rate distributions.

# 3 RESULTS AND DISCUSSION

Figure 3 illustrates the distribution of heat sources (Joule heat, non-radiative heat, and thermalization heat) in PSC with various absorbers: in $V = 0$ and $V_{oc}$ for $MASnI_3$, $MAPbI_3$, $CsPbI_3$, and $CsSnI_3$. According to the computed results, Joule heat phenomenon is the primary heat source in all of the simulated structures for V=0 (V), with heat primarily aggregating at the absorber/$TiO_2$ junction (900 nm) and thermalization heat is the main source of heating in the bulk of the absorber layers for $V = V_{oc}$ (V). Among the explored materials, $MASnI_3$ and $CsSnI_3$ have more thermal variation as heat generation increases rapidly in the absorber region (around 900 nm) especially in Joule and thermalization components in $V = 0$. Furthermore, as the voltage increases toward $V_{oc}$, the Joule heat component gradually decreases (according to Eq. (12) and $E = -\nabla\phi$) since the current density tends to zero $V = V_{oc}$ conditions. In contrast, the carrier recombination increases for $V = V_{oc}$ (higher forward bias), it leads to a rise in non-radiative recombination heating.

Figure 4 and Table 2 show the effects of thermal coupling on the electrical performance of four PSC types: $MASnI_3$, $MAPbI_3$, $CsPbI_3$, and $CsSnI_3$. The simulation results presented in this figure are the current density–voltage ($J$–$V$) characteristics and the values of key output parameters such as short-circuit current ($J_{sc}$), open-circuit voltage ($V_{oc}$), filling factor (FF), and PCE, with and without thermal coupling. There is a noticeable decrease in the $V_{oc}$ from 0.874 V to 0.845 V in the $MASnI_3$ PSC with reasonable thermal influence. The PCE is reduced from 18.424% to 17.552%. In this structure the $J_{sc}$ is not affected significantly (28.328 to 28.193 mA/cm$^2$), indicating that the loss in this

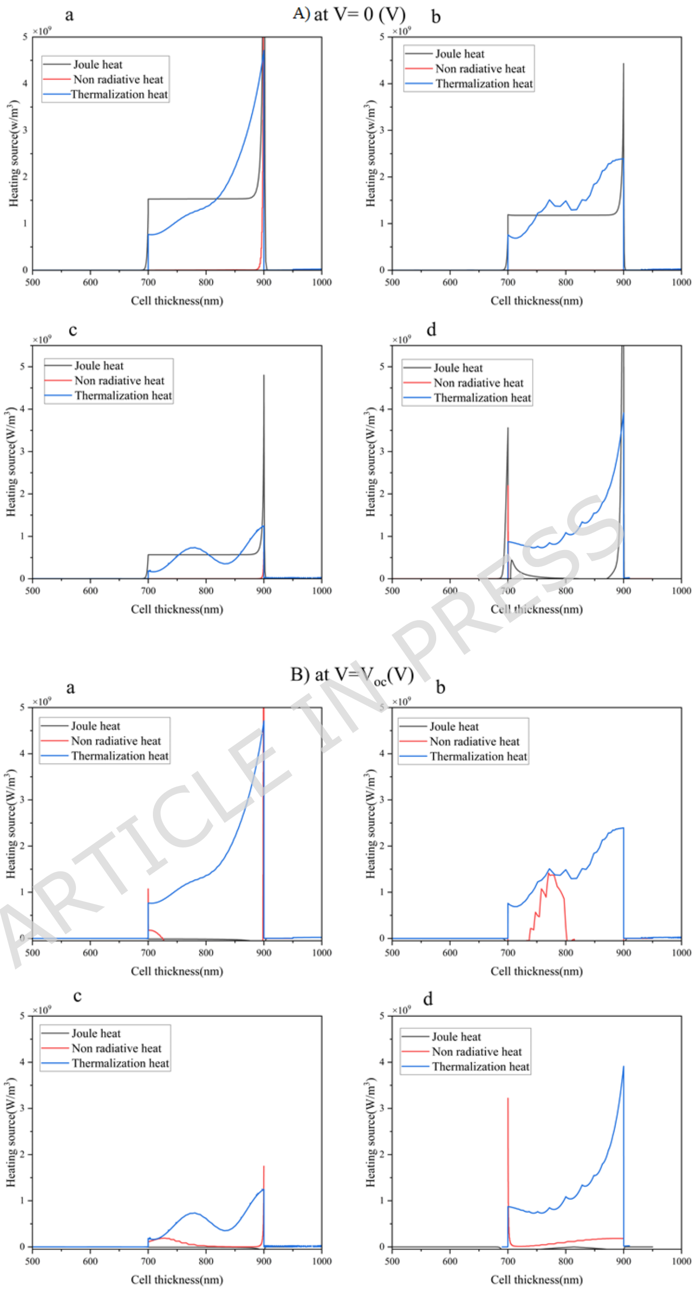

Figure 3: Heat generation sources within perovskite solar cells, including Joule heat, non-radiative recombination heat, and thermalization heat for different perovskite absorbers: (a) $MASnI_3$, (b) $MAPbI_3$, (c) $CsPbI_3$, and (d) $CsSnI_3$ for: A) $V = 0$ (V), B) $V = V_{oc}$ (V)

.

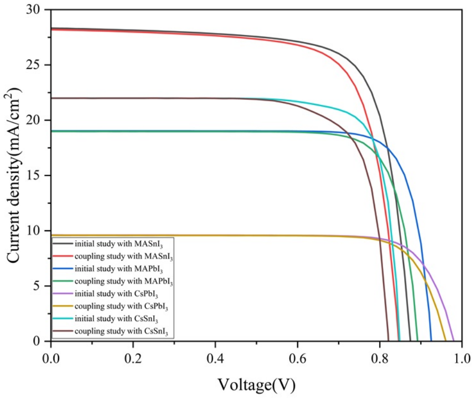

Figure 4: Voltage-current diagram for different absorption layers

Table 2: Comparison of key photovoltaic parameters ($V_{oc}$, $J_{sc}$, FF, and PCE) for perovskite solar cells with and without thermal coupling.

| **Cell/characteristics** | $\mathbf{J_{sc}}$ **(mA.cm$^{-2}$)** | $\mathbf{V_{oc}}$ **(V)** | **FF (%)** | **PCE (%)** |
|---|---|---|---|---|
| Initial study with MASnI$_3$ | 28.328 | 0.874 | 74.41 | 18.424 |
| Coupling study with MASnI$_3$ | 28.193 | 0.845 | 73.67 | 17.552 |
| Initial study with MAPbI$_3$ | 19.035 | 0.925 | 84.42 | 14.407 |
| Coupling study with MAPbI$_3$ | 18.981 | 0.899 | 79.87 | 13.63 |
| Initial study with CsPbI$_3$ | 9.466 | 0.951 | 81.31 | 7.32 |
| Coupling study with CsPbI$_3$ | 9.423 | 0.937 | 80.61 | 7.15 |
| Initial study with CsSnI$_3$ | 21.98 | 0.84 | 81.35 | 15.02 |
| Coupling study with CsSnI$_3$ | 21.98 | 0.82 | 75.73 | 13.65 |

material is dominated by the decrease in the value of $V_{oc}$. In the MAPbI$_3$ structure, the $V_{oc}$ is reduced from 0.925 V to 0.899 V, indicating that an increase in temperature leads to a reduction in $V_{oc}$. The decrease in PCE is from 14.407% to 13.63% in MAPbI$_3$. It is still lower in comparison with the loss in the performance of MASnI$_3$. The variation in the value $J_{sc}$ in this structure is negligible (19.035 to 18.981 mA/cm$^2$). The CsPbI$_3$ structure is stable in the sense that the $V_{oc}$ is decreased from 0.951 V to 0.937 V, with the lowest decrement among the three materials. The value of the decrease in the PCE is from 7.32% to 7.15%. This shows that this material is the least affected by heat. The variation of $J_{sc}$ is negligible (9.466 to 9.423 mA/cm$^2$) in this structure. $V_{oc}$ decreased from 0.84 V to 0.82 V in CsSnI$_3$, and the PCE decreased from 15.02% to 13.65% after thermal coupling. The variation in PCE indicates noticeable thermal influence compared with CsPbI$_3$. For a more detailed analysis of the temperature effects on the performance of PSCs, the changes in $V_{oc}$ and PCE were calculated and

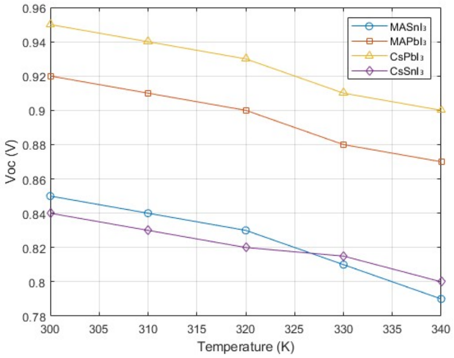

Figure 5: changes in Voc with temperature

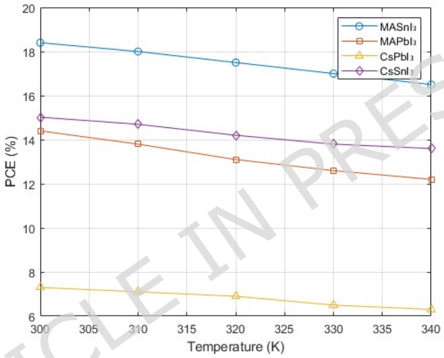

Figure 6: changes in PCE with temperature

reported separately.

Variations in $V_{oc}$ ($\Delta V_{oc}$) and PCE ($\Delta$PCE) are defined as:

$$\Delta V_{oc} = \frac{V_{\mathrm{oc,initial}} - V_{\mathrm{oc,coupled}}}{V_{\mathrm{oc,initial}}} \times 100 \tag{16}$$

$$\Delta \mathrm{PCE} = \frac{\mathrm{PCE}_{\mathrm{initial}} - \mathrm{PCE}_{\mathrm{coupled}}}{\mathrm{PCE}_{\mathrm{initial}}} \times 100 \tag{17}$$

where the initial parameters are calculated without the thermal effect feedback (T=293 K) and the coupled parameters are calculated by considering thermal effects.

A detailed analysis of the variations in $V_{oc}$ and PCE as a function of temperature has been performed based on Figures 5 and 6, and the corresponding data for four perovskite absorbers: $\mathrm{MASnI_3}$, $\mathrm{MAPbI_3}$, $\mathrm{CsPbI_3}$, and $\mathrm{CsSnI_3}$. Also, the changes in $V_{oc}$ and PCE are provided in the Tables3 and 4. For all materials, $V_{oc}$ decreases with increasing temperature; however, the rate of decrease

Table 3: Changes in open-circuit voltage ($\Delta V_{oc}$) for different perovskite absorbers.

| **Material** | **$\Delta V_{oc}$ (%)** | **$\Delta V_{oc}$ (V)** |
|---|---|---|
| $MASnI_3$ | 3.32% | 0.029 |
| $MAPbI_3$ | 2.81% | 0.026 |
| $CsPbI_3$ | 1.47% | 0.014 |
| $CsSnI_3$ | 2.38% | 0.020 |

Table 4: Changes in power conversion efficiency (ΔPCE) for different perovskite absorbers.

| **Material** | **ΔPCE (%)** | **ΔPCE** |
|---|---|---|
| $MASnI_3$ | 4.73% | 0.872 |
| $MAPbI_3$ | 5.39% | 0.777 |
| $CsPbI_3$ | 2.32% | 0.17 |
| $CsSnI_3$ | 9.12% | 1.37 |

differs among them. $MASnI_3$ and $MAPbI_3$ show the largest drop in $V_{oc}$, respectively, while $CsPbI_3$ presents the most temperature-stable performance with the least decrease. $CsSnI_3$ displays apparent temperature-dependent behavior under thermal coupling, showing a 2.38% drop in $V_{oc}$ and a 9.12% change in PCE, indicating higher temperature sensitivity than $CsPbI_3$ despite its high photovoltaic response. Similarly, the PCE of all absorbers declines with increasing temperature. While $MASnI_3$ has the highest initial efficiency but suffers deterioration at high temperatures. $CsPbI_3$ remains the most resistant against thermal degradation. These results confirm that the temperature-dependent performance of perovskite solar cells strongly depends on the absorber material. $CsPbI_3$ provides the best thermal resilience and $CsSnI_3$ suffers from high temperature sensitivity despite higher efficiency than $CsPbI_3$.

# 4 Conclusion

In this study, a detailed thermal analysis of perovskite solar cells (PSCs) was performed with special attention to three major heat generation mechanisms: Joule heat, non-radiative recombination heat, and thermalization heat. A coupled Opto-Electro-Thermal simulation framework was developed to study the thermal characteristics of the devices and their influence on photovoltaic performance.A comprehensive temperature-dependent analysis has been carried out to evaluate the variations in open-circuit voltage ($V_{oc}$) and power conversion efficiency (PCE) linked to four different perovskite absorbers: $MASnI_3$, $MAPbI_3$, $CsPbI_3$, and $CsSnI_3$. The analysis demonstrates that both parameters decrease with increasing temperature; however, the degradation rate strongly depends on the absorber composition. Among the studied materials, $CsPbI_3$ shows the highest thermal stability with the smallest decrease in both $V_{oc}$ and PCE, confirming its superior resistance to temperature-induced performance losses. On the other hand, $MASnI_3$ and $MAPbI_3$ show the largest decrease in $V_{oc}$ and efficiency due to their high sensitivity towards thermal degradation. $CsSnI_3$ exhibits higher temperature sensitivity despite its high photovoltaic response; its $V_{oc}$ drops by 2.38% and PCE varies by 9.12%, suggesting that its optoelectronic behavior under temperature variation is influenced by temperature-sensitive mechanisms such as carrier recombination and thermalization. In general, the results point out that the choice of the absorber material dictates the thermal stability of the PSC. $CsPbI_3$ is the most promising candidate for stable performance operation at elevated temperatures, while $CsSnI_3$ represents higher thermal sensitivity despite its high photovoltaic response.

# Author Contribution

M.R. and R.S. initiated the idea. M.R. and R.S. developed the concept. R.S. wrote the simulation algorithm and did the calculations and theoretical analysis. M.R. supervised the study. All authors discussed the content, analyzed the data, reviewed, and edited the manuscript.

# Funding

The authors declare that no funds, grants, or other support were received during the preparation of this manuscript.

# Data Availability

The data that support the findings of this study are available from the corresponding author on reasonable request.

# Code Availability

The code used in this study is available from the corresponding author upon reasonable request.

# References

[1] J. Y. Kim, J. Lee, H. Jung, H. Shin, and N. Park, "High-efficiency perovskite solar cells.," *Chemical reviews*, vol. 120 15, pp. 7867–7918, 2020.

[2] K. Afridi, M. Noman, and S. T. Jan, "Evaluating the influence of novel charge transport materials on the photovoltaic properties of masni3 solar

cells through scaps-1d modelling," *Royal Society Open Science*, vol. 11, 2024.

[3] A. Sheikh, R. Munir, M. A. Haque, A. Bera, W. Hu, P. Shaikh, A. Amassian, and T. Wu, "Effects of high temperature and thermal cycling on the performance of perovskite solar cells: Acceleration of charge recombination and deterioration of charge extraction.," *ACS applied materials & interfaces*, vol. 9 40, pp. 35018–35029, 2017.

[4] R. Cheacharoen, C. C. Boyd, G. F. Burkhard, T. Leijtens, J. A. Raiford, K. A. Bush, S. Bent, and M. McGehee, "Encapsulating perovskite solar cells to withstand damp heat and thermal cycling," *Sustainable Energy and Fuels*, vol. 2, pp. 2398–2406, 2018.

[5] Y. Liu, Y. Deng, Y. Chen, B. Chen, P. Guo, L. Chen, and Q. Zhang, "Investigation of internal thermal distribution in inverted perovskite solar cell and improvement of its heat dissipation performance," *Physica Scripta*, 2024.

[6] S. Zandi, P. Saxena, and N. E. Gorji, "Numerical simulation of heat distribution in rgo-contacted perovskite solar cells using comsol," *Solar Energy*, vol. 197, pp. 105–110, 2020.

[7] A. Hajjiah, "Heat dissipation in perovskite solar cells with different grain shapes," *Solar Energy*, vol. 293, p. 113479, 2025.

[8] M. Bahrami, M. M. Najafali, J. Maleki, F. Khalaji, M. Kanani, M. Moaddeli, and N. E. Gorji, "Heat generation in perovskite/cztsse tandem solar cells," *Sustainable Materials and Technologies*, vol. 43, p. e01308, 2025.

[9] A. Rostami, I. Tofigi, A. A. Barzinjy, and H. Mirtagioglu, "Theoretical modelling of high-efficiency perovskite solar cells and reduction of internal heat generation using hot-electron extraction," *Optical and Quantum Electronics*, vol. 54, no. 4, p. 234, 2022.

[10] A. Moradi, M. Maleki, S. R. Hosseini, M. Bahramgour, N. Delibas, and A. Niaei, "Thermal modeling of perovskite solar cells: Electron and hole transfer layers effects," *Optik*, vol. 302, p. 171683, 2024.

[11] S. Zandi, M. J. Seresht, A. Khan, and N. E. Gorji, "Simulation of heat loss in cu2znsn4sxse4-x thin film solar cells: A coupled optical-electrical-thermal modeling," *Renewable Energy*, vol. 181, pp. 320–328, 2022.

[12] N. Yang, F. Pei, J. Dou, Y. Zhao, Z. Huang, Y. Ma, S. Ma, C. Wang, X. Zhang, H. Wang, C. Zhu, Y. Bai, H. Zhou, T. Song, Y. Chen, and Q. Chen, "Improving heat transfer enables durable perovskite solar cells," *Advanced Energy Materials*, vol. 12, 2022.

[13] P. Saxena and N. E. Gorji, “Comsol simulation of heat distribution in perovskite solar cells: coupled optical–electrical–thermal 3-d analysis,” *IEEE Journal of Photovoltaics*, vol. 9, no. 6, pp. 1693–1698, 2019.

[14] S. B. Ivriq, M. H. Mohammadi, and R. S. Davidsen, “Enhancing photovoltaic efficiency in half-tandem mapbi3/masni3 perovskite solar cells with triple core-shell plasmonic nanoparticles,” *Scientific Reports*, vol. 15, no. 1, p. 1478, 2025.

[15] S. Zandi and M. Razaghi, “Finite element simulation of perovskite solar cell: A study on efficiency improvement based on structural and material modification,” *Solar Energy*, vol. 179, pp. 298–306, 2019.

[16] Y. Shen, F. Q. Wang, and Q. Wang, “Ultralow thermal conductivity and negative thermal expansion of cuscn,” *Nano Energy*, vol. 73, p. 104822, 2020.

[17] H. Ren, R. Yu, J. Qi, L. Zhang, Q. Jin, and D. Wang, “Hollow multishelled heterostructured anatase/tio2 (b) with superior rate capability and cycling performance,” *Advanced Materials*, vol. 31, no. 10, p. 1805754, 2019.

[18] L. Lin, L. Jiang, P. Li, H. Xiong, Z. Kang, B. Fan, and Y. Qiu, “Simulated development and optimized performance of cspbi3 based all-inorganic perovskite solar cells,” *Solar Energy*, vol. 198, pp. 454–460, 2020.

[19] Y. Gan, D. Zhao, B. Qin, X. Bi, Y. Liu, W. Ning, R. Yang, and Q. Jiang, “Numerical simulation of high-performance cspbi3/fapbi3 heterojunction perovskite solar cells,” *Energies*, vol. 15, no. 19, p. 7301, 2022.

[20] W. Lee, H. Li, A. B. Wong, D. Zhang, M. Lai, Y. Yu, Q. Kong, E. Lin, J. Urban, J. Grossman, and P. Yang, “Ultralow thermal conductivity in all-inorganic halide perovskites,” *Proceedings of the National Academy of Sciences*, vol. 114, pp. 8693 – 8697, 2017.

[21] M. Morimoto, S. Kawano, S. Miyamoto, K. Miyazaki, S. Hayase, and S. Iikubo, “Electronic structure and thermal conductance of the masni3/bi2te3 interface: a first-principles study,” *Scientific reports*, vol. 12, no. 1, p. 217, 2022.

[22] J. Ball, S. Stranks, M. T. Hörantner, S. Hüttner, W. Zhang, E. J. W. Crossland, I. R. Ramirez, M. Riede, M. Johnston, R. Friend, and H. Snaith, “Optical properties and limiting photocurrent of thin-film perovskite solar cells,” *Energy and Environmental Science*, vol. 8, pp. 602–609, 2015.

[23] M. Moradbeigi and M. Razaghi, “Investigation of optical and electrical properties of novel 4t all perovskite tandem solar cell,” *Scientific reports*, vol. 12, no. 1, p. 6733, 2022.

[24] G. Donnarumma, J. Woźny, and Z. Lisik, "Numerical solution of the anisotropic poisson equation for sic semiconductors device simulation," *Materials Science and Engineering B-advanced Functional Solid-state Materials*, vol. 176, pp. 293–296, 2011.

[25] P. Jindal, B. S. Kumar, and J. Bhattacharya, "Coupled electrochemical-abuse-heat-transfer model to predict thermal runaway propagation and mitigation strategy for an ev battery module," *Journal of Energy Storage*, 2021.

[26] M. Jiang, W. Zhang, and J. Tang, "Transient performance modelling of ultra-thin sn-based perovskite solar cells based on electrode contact design to improve thermal stability," *The European Physical Journal Plus*, vol. 137, no. 8, p. 978, 2022.

[27] A. Shang and X. Li, "Photovoltaic devices: opto-electro-thermal physics and modeling," *Advanced Materials*, vol. 29, no. 8, p. 1603492, 2017.